Field-free Josephson diode effect in altermagnet/normal metal/altermagnet junctions

Qiang Cheng [1,2,*] Yue Mao [2] and Qing-Feng Sun [2,3,†]

[1]*School of Science, Qingdao University of Technology, Qingdao, Shandong 266520, China*

[2]*International Center for Quantum Materials, School of Physics, Peking University, Beijing 100871, China*

[3]*Hefei National Laboratory, Hefei 230088, China*

(Received 4 April 2024; revised 9 June 2024; accepted 11 July 2024; published 25 July 2024)

The field-free and highly efficient diodes with the nonreciprocity of supercurrent are believed to be the core block of superconducting computing devices without dissipation. In this paper, we propose a Josephson diode based upon altermagnets with vanishing net macroscopic magnetization. The nonreciprocity of supercurrent can be realized without applying any external magnetic field or ferromagnetic exchange field, which can avoid the magnetic cross-talk between the basic elements of the devices. A high efficiency exceeding 40% can be obtained, and the efficiency shows high stability when the structure parameters are changed. The diode efficiency is antisymmetric about the relative orientation angle of the superconducting leads, so that its sign can easily be inverted by adjusting the relative orientation angle. The symmetries satisfied by the current-phase difference relations and the diode efficiency are analyzed by considering the transformations of the junctions under the time reversal, the spin rotation, and the mirror reflection operations. The high efficiency and the high stability of the Josephson diode effect in our junctions make it possible to design field-free dissipationless diode devices.

DOI: 10.1103/PhysRevB.110.014518

I. INTRODUCTION

The nonreciprocity of supercurrent with different critical currents for opposite directions paves the way for the design of nondissipative digital logic, which has attracted a great deal of attention [1–19]. In particular, the nonreciprocity of supercurrent in Josephson junctions, i.e., the Josephson diode effect (JDE), has stimulated growing interest due to the design and construction flexibility of the junctions. The experimental observations of the JDE have been reported recently [20–27]. In $NbSe_2/Nb_3Br_8/NbSe_2$ junctions, the stable half-wave rectification of a square-wave excitation has been realized using a very low switching current [20]. Other involved structures include Josephson junctions based on InAs quantum wells [21–23], type-II Dirac semimetal [24], magic-angle twisted bilayer graphene [25] and a single magnetic atom [26]. The non-locally-controlled JDE is also detected experimentally in Josephson junctions with short-range coherent coupling [27].

In addition to these experiments, various theoretical schemes for the JDE have been proposed [28–49]. For example, a metallic nanowire on top of two superconducting slabs can host a nonreciprocal supercurrent when finite-momentum Cooper pairing is induced by screening currents [32]. The JDE with high efficiency is predicted in supercurrent interferometers composed of two Josephson junctions [36]. The tunable JDE is theoretically shown on the surface of a topological insulator with an applied magnetic field [44]. The minimal theoretical model for the JDE is formulated in two-dimensional electron gas with a ferromagnetic barrier [45]. The controllable JDE by the magnetic configuration of the barriers is also studied in Andreev molecules [48]. Although the JDE has been examined in various Josephson structures both experimentally and theoretically, an external magnetic field or the exchange field from a ferromagnet is always required for most of the existing studies to cause the time-reversal symmetry breaking necessary for the formation of the JDE. This will bring about the inevitable competition between magnetization and superconductivity in Josephson junctions. Furthermore, the presence of an external magnetic field or a stray magnetic field produced by a ferromagnet will cause magnetic cross-talk between the basic elements of the logic device [50]. The magnetic cross-talk is a negative factor for realistic applications of the JDE, and it needs to be avoided, especially in the design of a high-density device [51].

Recently, altermagnetism, as the third magnetic phase, has become a hot topic in condensed-matter physics [52–60]. Altermagnet (AM) breaks time-reversal symmetry, similar to ferromagnetism, but it possesses vanishing macroscopic net magnetization due to the alternating order of the magnetic moments in both direct space and momentum space [53–55] [see Fig. 1(a)]. The absence of macroscopic net magnetization in altermagnetism prevents the emergence of a stray magnetic field, which is very prevalent in structures including ferromagnets. This makes AMs an ideal magnetic material in the design and construction of heterojunctions consisting of AMs and superconductors (SCs). Andreev reflection [61,62], the dc Josephson effect [60,63,64], and the Majorana corner modes [65,66] in the heterostructures comprising AMs and SCs have been recently studied based on the zero net magnetization of AMs. In particular, the crystalline orientation-dependent transport properties are clarified in Refs. [60–64], which originate from the anisotropic spin polarization in AMs.

*Contact author: chengqiang07@mails.ucas.ac.cn

†Contact author: sunqf@pku.edu.cn

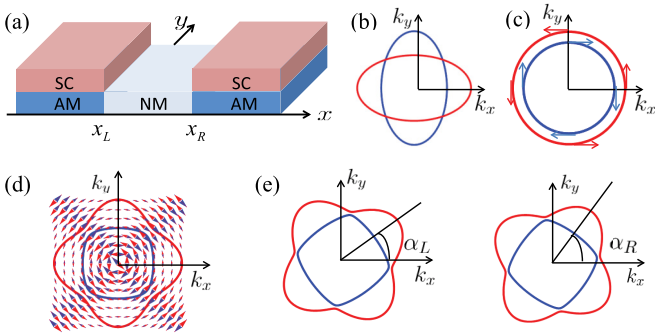

FIG. 1. (a) Schematic illustration of AMSC/NM/AMSC Josephson junctions based upon d-wave AMs. (b) The elliptical Fermi surfaces of the normal state of AMSCs with altermagnetism but without RSOC. The blue (red) ellipse is occupied by spin-up (spin-down) electrons. (c) The Fermi surfaces of the normal state of AMSCs with RSOC but without altermagnetism. The blue and red arrows denote electron spin under spin-momentum locking. (d) The Fermi surfaces for the normal state of AMSCs with both altermagnetism and RSOC. The averages of the in-plane spin of electrons are denoted by arrows. (e) The Fermi surfaces for the normal state of the left (right) AMSC with an orientation angle $\alpha_{l(r)}$.

In this paper, we propose a theoretical scheme for the JDE in junctions with a normal metal (NM) sandwiched between two AM-based SCs (AMSCs), i.e., the AMSC/NM/AMSC Josephson junctions, as shown in Fig. 1(d). The JDE in our junctions is derived from the simultaneous breaking of time-reversal symmetry and in-plane inversion symmetry. The former is caused by anisotropic d-wave altermagnetism with zero macroscopic net magnetization in AMSCs, while the latter is caused by Rashba spin-orbit coupling (RSOC) and the mismatch of the crystallographic orientation in AMSCs. Any external magnetic field or ferromagnetic exchange field is not needed for the nonreciprocity of supercurrent in our junctions, and the emergence of a stray field is completely avoided. A high diode efficiency is achieved and can be maintained in a large range of the junction parameters. The efficiency exhibits an antisymmetric property about the relative orientation angle of AMSCs, and its sign can also be inverted by altering the magnitudes of altermagnetism and RSOC. We also analyze the current-phase difference relations (CPRs) and the diode efficiency from the viewpoint of symmetry through considering the transformations of the junctions under time reversal, spin rotation, and mirror reflection as well as their joint operations. The results obtained in this work will be helpful in practical applications of the field-free superconductor diode with low energy consumption.

II. MODEL AND FORMULATION

The AMSC/NM/AMSC Josephson junctions based upon d-wave AMs in the xy plane considered by us are schematically shown in Fig. 1(a). The left and right semi-infinite AMSCs are formed through coupling AMs to bulk SCs with a circular Fermi surface and isotropic s-wave pairing. In addition to altermagnetism, RSOC in AMSCs is assumed due to the breaking of the out-of-plane mirror reflection. Before proceeding further, we now discuss comprehensively the electric structures of the normal state of AMSCs for different situations. The Hamiltonian for the normal state of AMSCs is shown in Eq. (A1) in Appendix A. For the normal state of AMSCs with altermagnetism but without RSOC, the Fermi surfaces are two ellipses that are occupied by electrons with opposite spin, i.e., the out-of-plane spin-up and the out-of-plane spin-down, as shown in Fig. 1(b). For the normal state of AMSCs with RSOC but without altermagnetism, the Fermi surfaces are two concentric circles with in-plane spin-momentum locking, as shown in Fig. 1(c). For the coexistence of altermagnetism and RSOC, the Fermi surfaces for the normal state are two closed curves, as shown in Fig. 1(d). In this situation, the electron spin will possess both in-plane and out-of-plane components. The blue and red arrows, denoting the averages of the in-plane spin of electrons in momentum space, are calculated from the eigenvector on the Fermi surface with the same color as shown in Fig. 1(d). The calculation details can be found in Appendix A.

In this paper, we will consider AMSCs not only with the coexistence of altermagnetism and RSOC but also with different orientation angles. The orientation of the left (right) AMSC is characterized by $\alpha_{l(r)}$, which is defined as the angle between the crystalline axis of the left (right) AMSC and the interface normal [see Fig. 1(e)]. The Fermi surfaces for the normal states of the left and right AMSCs are shown schematically in Fig. 1(e), which can be obtained by rotating the Fermi surfaces in Fig. 1(d) about the z axis by the α_L angle and the α_R angle, respectively. After the rotations, corresponding changes will also occur for the spin direction of electrons. Detailed discussions on the electric structure of the normal state of AMSCs after rotation can be found in Appendix A. The central region of the junctions is a conventional NM without both altermagnetism and RSOC. The two interfaces for the junctions are located at $x = x_L$ and $x = x_R$, which are parallel to the y axis as shown in Fig. 1(a). The Josephson current flows along the direction parallel to the x axis. Next, we will use Δx to denote the length of NM, i.e., $\Delta x = x_R - x_L$.

The Bogoliubov–de Gennes (BdG) Hamiltonian for the left (right) AMSC in the region $x < x_L$ ($x > x_R$) is given by $H_{L(R)} = \sum_{\mathbf{k}} \psi^+_{L(R)}(\mathbf{k}) \check{H}_{L(R)}(\mathbf{k}) \psi_{L(R)}(\mathbf{k})$, with $\psi_{L(R)}(\mathbf{k}) = (c_{L(R)\mathbf{k}\uparrow}, c_{L(R)\mathbf{k}\downarrow}, c^+_{L(R)-\mathbf{k}\uparrow}, c^+_{L(R)-\mathbf{k}\downarrow})^T$ and

$$\check{H}_{L(R)}(\mathbf{k}) = \check{H}_0(\mathbf{k}) + \check{H}_J(\mathbf{k}) + \check{H}_\lambda(\mathbf{k}) + \check{H}_\Delta(\mathbf{k}) \tag{1}$$

in the particle-hole $\otimes$ spin space. The four terms in Eq. (1) are expressed as

$$\begin{aligned}
\check{H}_0(\mathbf{k}) &= \left[t_0\left(k_x^2 + k_y^2\right) - \mu\right]\tau_z \otimes \sigma_0, \\
\check{H}_J(\mathbf{k}) &= t_J\left[\left(k_x^2 - k_y^2\right)\cos 2\alpha_{l(r)} + 2k_x k_y \sin 2\alpha_{l(r)}\right]\tau_z \otimes \sigma_z, \\
\check{H}_\lambda(\mathbf{k}) &= \lambda[(k_y \cos\alpha_{l(r)} - k_x \sin\alpha_{l(r)})\tau_0 \otimes \sigma_x \\
&\quad - (k_x \cos\alpha_{l(r)} + k_y \sin\alpha_{l(r)})\tau_z \otimes \sigma_y], \\
\check{H}_\Delta(\mathbf{k}) &= -\Delta_0[\cos\phi_{l(r)}\tau_y + \sin\phi_{l(r)}\tau_x] \otimes \sigma_y,
\end{aligned} \tag{2}$$

which describes the kinetic energy of particles, the d-wave altermagnetism, the spin-orbit coupling, and the superconducting gap matrix, respectively. Here, t_J, λ, and Δ_0 are the magnitudes of altermagnetism, RSOC, and the superconducting gap. $\mathbf{k} = (k_x, k_y)$ is the two-dimensional wave vector in the junctions plane. $\phi_{l(r)}$ is the superconducting phase of the

left (right) AMSC, and the phase difference will be defined as $\phi = \phi_l - \phi_r$. We have used τ_x, τ_y, τ_z, τ_0 and σ_x, σ_y, σ_z, σ_0 to denote the three components of the Pauli matrices and the identity matrices in particle-hole space and spin space, respectively. From Eq. (2), one can find that $\hat{H}_J(\mathbf{k})$ is proportional to $\tau_z \otimes \sigma_z$, which implies that particles and holes will experience the opposite effects of altermagnetism. In this paper, we chose the simplest d-wave altermagnetism as given in Eq. (2) to demonstrate the JDE based upon AMs, although AMs with higher powers of k_x and k_y, such as the g-wave AMs [53], also satisfy the necessary conditions for the JDE. The BdG Hamiltonian for NM in the central region ($x_L < x < x_R$) can be written as $H_N = \sum_{\mathbf{k}} \psi_N^+(\mathbf{k}) \check{H}_0(\mathbf{k}) \psi_N(\mathbf{k})$, with $\psi_N(\mathbf{k}) = (c_{N\mathbf{k}\uparrow}, c_{N\mathbf{k}\downarrow}, c^+_{N-\mathbf{k}\uparrow}, c^+_{N-\mathbf{k}\downarrow})^T$ and the kinetic energy term $\check{H}_0(\mathbf{k}) = [t_0(k_x^2 + k_y^2) - \mu]\tau_z \otimes \sigma_0$.

To calculate the Josephson current in the junctions, we can discretize the Hamiltonians $H_{L(R)}$ and H_N on a two-dimensional square lattice with the lattice constant a (see Appendix B). The discrete Hamiltonian can be given by [67]

$$H = \sum_{\mathbf{i}} \big[\psi_{\mathbf{i}}^+ \check{H} \psi_{\mathbf{i}} + \psi_{\mathbf{i}}^+ \check{H}_x \psi_{\mathbf{i}+\delta_x} + \psi_{\mathbf{i}}^+ \check{H}_y \psi_{\mathbf{i}+\delta_y} + \psi_{\mathbf{i}}^+ \check{H}_{xy} \psi_{\mathbf{i}+\delta_x+\delta_y} + \psi_{\mathbf{i}}^+ \check{H}_{x\bar{y}} \psi_{\mathbf{i}+\delta_x-\delta_y} + \text{H.c.}\big]. \quad (3)$$

Here, $\mathbf{i} = (i_x, i_y)$ denotes the position of sites in the lattice, with i_y being limited in $1 \leqslant i_y \leqslant N_y$. The width W of the junctions satisfies $W = (N_y - 1)a$. The subscripts $\mathbf{i} + \delta_x$ and $\mathbf{i} + \delta_y$ represent the nearest-neighbor sites of the $\mathbf{i}$th site along the x direction and the y direction, respectively. The subscripts $\mathbf{i} + \delta_x + \delta_y$ and $\mathbf{i} + \delta_x - \delta_y$ represent the next-nearest-neighbor sites of the $\mathbf{i}$th site. For the left (right) AMSC, one has $i_x \leqslant 0$ ($i_x \geqslant N_x + 1$). The operator $\psi_{\mathbf{i}}$ is expressed as $\psi_{\mathbf{i}} = (\psi_{L(R)\mathbf{i}\uparrow}, \psi_{L(R)\mathbf{i}\downarrow}, \psi^+_{L(R)\mathbf{i}\uparrow}, \psi^+_{L(R)\mathbf{i}\downarrow})^T$ in the left (right) AMSC. For NM, one has $1 \leqslant i_x \leqslant N_x$ and its length Δx satisfies $\Delta x = N_x a$. The operator $\psi_{\mathbf{i}}$ in NM is expressed as $\psi_{\mathbf{i}} = (\psi_{N\mathbf{i}\uparrow}, \psi_{N\mathbf{i}\downarrow}, \psi^+_{N\mathbf{i}\uparrow}, \psi^+_{N\mathbf{i}\downarrow})$. The explicit expressions of the matrices $\check{H}$, $\check{H}_x$, $\check{H}_y$, $\check{H}_{xy}$, and $\check{H}_{x\bar{y}}$ for the left AMSC, the right AMSC, and the central NM can be found in Appendix B.

The Hamiltonian describing the hopping between different regions can be given by

$$H_T = \sum_{1 \leqslant i_y \leqslant N_y} \big[\psi^+_{(0,i_y)} \check{T}_L \psi_{(1,i_y)} + \psi^+_{(N_x+1,i_y)} \check{T}_R \psi_{(N_x,i_y)} + \text{H.c.}\big], \quad (4)$$

with the hopping matrix $\check{T}_{L(R)} = \text{diag}(te^{-i\phi_{l(r)}/2}, te^{-i\phi_{l(r)}/2}, -te^{i\phi_{l(r)}/2}, -te^{i\phi_l(r)/2})$. When we write Eqs. (3) and (4), a unitary transformation has been performed. Then, the superconducting phases ϕ_l and ϕ_r for the left and right AMSCs in Eq. (3) have been eliminated and they will appear in the hopping matrix $\check{T}_{L(R)}$ in Eq. (4). The details for the transformation can be found in Appendix B.

The particle number operator in the left AMSC can be written as

$$N = \sum_{i_x \leqslant 0, i_y} \sum_{\sigma=\uparrow,\downarrow} \psi^+_{\mathbf{i}\sigma} \psi_{\mathbf{i}\sigma}. \quad (5)$$

Using the Green function method, the Josephson current can be expressed as [67–69]

$$I = e\left\langle \frac{dN}{dt} \right\rangle = -\frac{e}{2\pi} \int dE \, \text{Tr}[\Gamma_z \check{T}_L G^<_{NL}(E) + \text{H.c.}], \quad (6)$$

with $\Gamma_z = \sigma_z \otimes 1_{2\times 2}$. From the fluctuation-dissipation theorem, the lesser Green function $G^<_{NL}(E)$ can be expressed as $G^<_{NL}(E) = -f(E)[G^r_{NL}(E) - G^a_{NL}(E)]$ with the Fermi distribution function $f(E)$. The retarded Green function $G^r_{NL}(E)$ and the advanced Green function $G^a_{NL}(E)$ can be derived from the matrices $\check{H}$, $\check{H}_x$, $\check{H}_y$, $\check{H}_{xy}$, and $\check{H}_{x\bar{y}}$ in Eq. (3). The details of the derivation process are presented in Appendix B.

III. NUMERICAL RESULTS AND DISCUSSIONS

Before presenting the numerical results, we give the necessary conditions responsible for the JDE in the AMSC/NM/AMSC junctions from the symmetry analysis (see Appendix C for details) [70]. For $t_J = 0$ and $\lambda \neq 0$, there is only RSOC in AMSCs, and altermagnetism is absent. The junctions will respect the time-reversal symmetry. The continuum Hamiltonian for the left (right) AMSC can be transformed according to $\mathcal{T} H_{L(R)}(\alpha_{l(r)}, \phi_{l(r)}) \mathcal{T}^{-1} = H_{L(R)}(\alpha_{l(r)}, -\phi_{l(r)})$ by the time-reversal operator $\mathcal{T}$. Since the time-reversal operation will invert the direction of the Josephson current, we have the following relation for CPRs:

$$I(\alpha_l, \alpha_r, \phi) = -I(\alpha_l, \alpha_r, -\phi). \quad (7)$$

This relation means that the positive current and the negative current possess the same critical value, and the JDE cannot be expected while $t_J = 0$. On the other hand, for $t_J \neq 0$ and $\lambda = 0$, there is only altermagnetism in AMSCs, and RSOC is absent. The time-reversal symmetry will be broken due to the presence of altermagnetism. However, the symmetry under the joint operation $\mathcal{X} = \mathcal{R}_y(\pi)\mathcal{T}$ will be satisfied by AMSCs with $\mathcal{R}_y(\pi)$ being the spin rotation about the y axis by a π angle. The Hamiltonian for the left (right) AMSC will be transformed according to $\mathcal{X} H_{L(R)}(\alpha_{l(r)}, \phi_{l(r)}) \mathcal{X}^{-1} = H_{L(R)}(\alpha_{l(r)}, -\phi_{l(r)})$. In this situation, the relation in Eq. (7) can be obtained again and the JDE in our junctions will be forbidden. From the above discussions, the coexistence of RSOC and altermagnetism is a necessary condition for the possible emergence of the JDE in the AMSC/NM/AMSC junctions.

Another condition for the JDE is the unequal orientation angles in the left AMSC and the right AMSC. To prove this point, we introduce the in-plane inversion operation $\mathcal{Y} = \mathcal{M}_{xz}\mathcal{M}_{yz}$. Here, $\mathcal{M}_{xz}$ and $\mathcal{M}_{yz}$ are the mirror reflection operations about the xz plane and the yz plane, respectively. The in-plane inversion operation can transform the Hamiltonian for the left (right) AMSC according to $\mathcal{Y} H_{L(R)}(\alpha_{l(r)}, \phi_{l(r)}) \mathcal{Y}^{-1} = H_{R(L)}(\alpha_{l(r)}, \phi_{l(r)})$. The operation $\mathcal{M}_{yz}$ exchanged the orientation angles and the superconducting phases for the left AMSC and the right AMSC. As a result, the Josephson current is inverted and the relation $I(\alpha_l, \alpha_r, \phi) = -I(\alpha_r, \alpha_l, -\phi)$ will hold. If $\alpha_l = \alpha_r = \alpha$, the relation in Eq. (7) will be satisfied and the JDE will also be

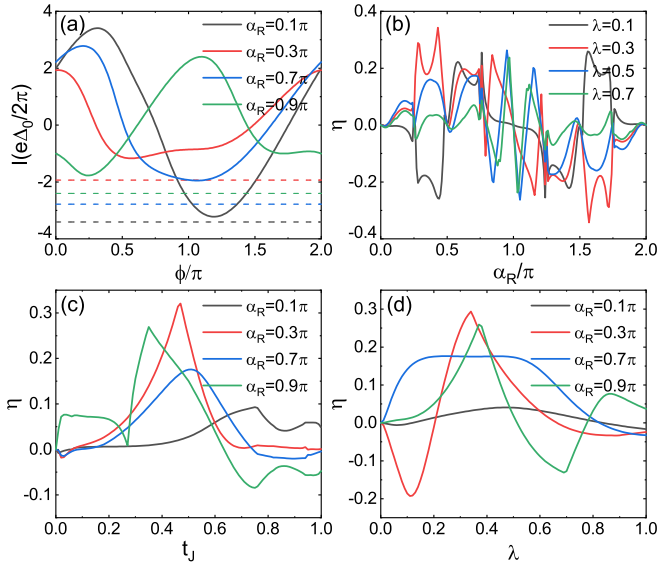

FIG. 2. (a) The CPRs for different orientation angles with $t_J = 0.5$ and $\lambda = 0.3$. Each dashed line gives the critical current $-I_{C+}$ of the CPR with the same color. (b) The variations of the diode efficiency as the orientation angle for $t_J = 0.5$. (c) The variations of the diode efficiency as the magnitude of altermagnetism for $\lambda = 0.3$. (d) The variations of the diode efficiency as RSOC strength λ for $t_J = 0.5$. Other parameters are taken as $t_0 = 1$, $t = 1$, $\mu = 2$, $a = 1$, $N_x = 1$, and $N_y = 3$.

forbidden. In other words, the orientation angles for the left AMSC and the right AMSC must be different in order to break the in-plane inversion symmetry and produce the JDE.

Next, we will present the numerical results with the two necessary conditions for the JDE being simultaneously satisfied. In our calculations, we will fix $\alpha_l = 0$ for definiteness and let α_R vary. Other parameters are taken as $t_0 = 1$, $\mu = 2$, $t = 1$, $\Delta_0 = 0.01$, and $a = 1$. Figure 2(a) shows the CPRs for different values of α_r with $t_J = 0.5$ and $\lambda = 0.3$. For each CPR curve, we define the critical value for its positive current as I_{c+} with $I_{c+} = \max[I(0 < \phi < 2\pi)]$ and the critical value for its negative current as I_{c-} with $I_{c-} = \max[-I(0 < \phi < 2\pi)]$. In Fig. 2(a), we plot $-I_{c+}$ of the CPRs as dashed lines. Each dashed line and its corresponding CPR curve possess the same color. It is found that the dashed lines are not tangent with their CPR curves. This indicates that the critical value for the positive current and that for the negative current are not equal, i.e., $I_{c+} \neq I_{c-}$. This is just the nonreciprocity effect of the Josephson supercurrent in our junctions. Actually, all the dashed lines in Fig. 2(a) are below their corresponding CPRs, and one has $I_{c-} < I_{c+}$. As a result, our junctions with a fixed orientation of the right AMSC can serve as an efficient rectifier by altering the direction of the applied current I with $I_{c-} < I < I_{c+}$.

To measure the nonreciprocity in our junctions, we introduce the Josephson diode efficiency η, which is defined as

$$\eta = \frac{I_{c+} - I_{c-}}{I_{c+} + I_{c-}}. \tag{8}$$

The diode efficiency η as functions of α_r is shown in Fig. 2(b) for different values of RSOC with $t_J = 0.5$. The efficiency η exhibits oscillation behavior when the orientation angle α_r is adjusted. However, η can keep stable and high values in a large range of α_r. For example, the efficiencies for $\lambda = 0.1$ and 0.3 can reach about 20% in the range of $0.25\pi < \alpha_r < 0.5\pi$ and can exceed 15% in the range of $0.5\pi < \alpha_r < 0.75\pi$. The stable and high efficiency with no strict demand on the value of the orientation angle in our junctions will be helpful for the practical applications of the JDE based upon AMs. From Fig. 2(b), one can also find that raising the value of RSOC will not always increase the efficiency for the given t_J. For example, the efficiency in the angle range of $0.25\pi < \alpha_r < 0.5\pi$ is obviously weakened when the value of RSOC is increased from $\lambda = 0.3$ to 0.5 and then to $\lambda = 0.7$. On the contrary, the smaller value $\lambda = 0.1$ of RSOC can cause higher diode efficiency in the same angle range. The large value of RSOC is not the essential condition for the high diode efficiency, which is another advantage of our junctions.

In addition, the curves for the efficiency η in Fig. 2(b) satisfy the following relation:

$$\eta(\alpha_r) = -\eta(2\pi - \alpha_r), \tag{9}$$

which suggests that the diode efficiency will change its sign when one adjusts the orientation angle from α_r to $-\alpha_r$. To clarify the relation in Eq. (9), we introduce the joint operation $\mathcal{Z} = \mathcal{T}\mathcal{M}_{xz}$ (see Appendix C for details). The Hamiltonian $H_{L(R)}$ for the left (right) AMSC will be transformed according to $\mathcal{Z}H_{L(R)}(\alpha_{l(r)}, \phi_{l(r)})\mathcal{Z}^{-1} = H_{L(R)}(2\pi - \alpha_{l(r)}, -\phi_{l(r)})$ under the joint operation. As a unitary operation, the mirror reflection $\mathcal{M}_{xz}$ does not change the Josephson current. On the other hand, the time-reversal operation $\mathcal{T}$ only inverts the direction of the current. Hence, we have the relation $I(\alpha_l, \alpha_r, \phi) = -I(2\pi - \alpha_l, 2\pi - \alpha_r, -\phi)$ for CPRs. For $\alpha_l = 0$, the relation will degenerate into $I(\alpha_r, \phi) = -I(2\pi - \alpha_r, -\phi)$. When one adjusts the orientation angle from α_r to $-\alpha_r$, the positive (negative) current for α_r will become the negative (positive) current for $-\alpha_r$. The critical value $I_{c+}(I_{c-})$ for α_r will turn into the critical value $I_{c-}(I_{c+})$. According to the definition of η in Eq. (8), η will change its sign when α_r is changed into $-\alpha_r$. Furthermore, for $\alpha_r = \pi$, we have $I(\pi, \phi) = -I(\pi, -\phi)$ and the JDE will vanish as shown in Fig. 2(b).

The variations of the efficiency η as the magnitude of altermagnetism are presented in Fig. 2(c) for several given values of the orientation angle α_r. In Fig. 2(c), we have taken $\lambda = 0.3$. For the orientation angle $\alpha_r = 0.3\pi$, 0.7π, or 0.9π, the efficiency η reaches its peak value at the position around $t_J = 0.4$. The peak value can exceed 15%, 25%, and even 30% for $\alpha_r = 0.3\pi$, 0.7π, and 0.9π. In particular, a diode efficiency exceeding 10% can be obtained in a large range of t_J for the three orientation angles, which shows the excellent stability of the diode effect in our AMSC/NM/AMSC junctions when the strength of altermagnetism is changed. The variations of efficiency η as RSOC are presented in Fig. 2(d) for the given orientation angles and the fixed $t_J = 0.5$. A similar stability can also be found in Fig. 2(d) for these orientation angles when the strength of RSOC is altered. In particular, it is found that the very small value of RSOC can bring about high efficiency. For $\alpha_r = 0.3\pi$ and 0.7π, an efficiency of about 10% can be achieved even for $\lambda = 0.05$, which is one-tenth of t_J. In Figs. 2(c) and 2(d), we also consider the variations of η for the small orientation angle $\alpha_r = 0.1\pi$. In this situation,

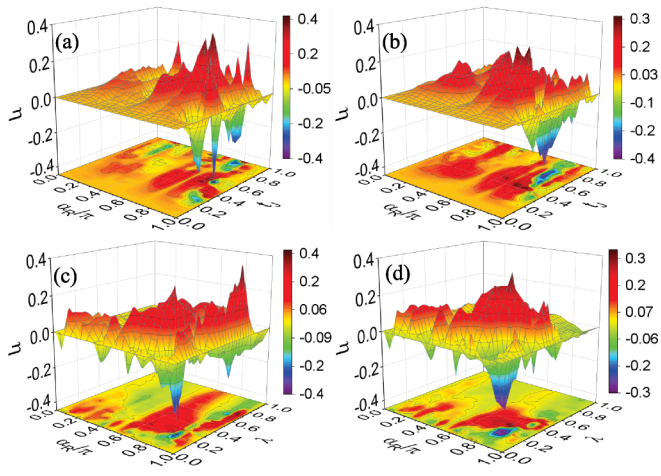

FIG. 3. The Josephson diode efficiency η for (a) $N_x = 1$ and (b) $N_x = 10$ in the (α_R, t_J) space and for (c) $N_x = 1$ and 10 in the (α_R, λ) space. For the width of the junctions, we have taken $N_y = 15$. In (a) and (b), λ is taken as 0.3; in (c) and (d), t_J is taken as 0.5.

a larger value of altermagnetism or RSOC is needed for the appearance of the peak value of η, which corresponds to the unobvious in-plane inversion symmetry breaking for the small orientation mismatch of AMSCs. In addition, adjusting the strength of altermagnetism or RSOC can change the sign of η as shown in Figs. 2(c) and 2(d); this can also be observed in Fig. 2(b).

In Fig. 2, we have taken $N_y = 3$, which corresponds to the narrow limit of the junctions. For the discrete model in Eq. (3), the next-neighbor hopping is required in order to describe the altermagnetism in AMSCs. The junctions with $N_y = 3$ are enough to seize the basic physics in our Josephson structure based upon AMs. However, for practical applications, it is necessary to consider the influence of the width of the junctions on the JDE. In Fig. 3(a), we present the diode efficiency η for $N_y = 15$ as a bivariate function of α_R and t_J and its projection on the (α_R, t_J) plane. It is found that the peak value of η can exceed 36% and the valley value of η is less than -44%. The obtained high efficiency implies that an increase in the width of the AMSC/NM/AMSC junctions will not weaken the JDE. From the projection of η, one can also find that the parameters for the high efficiency distribute in a large area in the (α_R, t_J) plane. The area is approximately centered around the point with $\alpha_R = 0.8\pi$ and $t_J = 0.4$ as shown in Fig. 3(a). The similar property of the diode efficiency can manifest itself in Fig. 3(c) when η is expressed as a bivariate function of α_R and λ. In this situation, the peak value of η will exceed 37% and the valley value can reach -39%. The parameters α_R and λ for the high efficiency mainly distribute around the point with $\alpha_R = 0.7\pi$ and $\lambda = 0.3$ in the (α_R, λ) plane. The above discussions on the numerical results in Figs. 3(a) and 3(c) indicate the high stability and the high efficiency of the JDE in the AMSC/NM/AMSC junctions when the width of the junctions is increased. Next, we discuss the influence of the length of the junctions on the JDE. In Figs. 3(a) and 3(c), we have taken $N_x = 1$, which corresponds to the short limit of the junctions. In Figs. 3(b) and 3(d), the numerical results of the efficiency η for $N_x = 10$ are presented as functions of (α_R, t_J) and (α_R, λ), respectively. The increase of the length will not significantly weaken the diode efficiency. The peak value and the valley value of η in Fig. 3(b) can reach about 32% and -38% while those values in Fig. 3(d) can reach about 37% and -32%. Although the distribution area of the parameters responsible for the high efficiency in Fig. 3(d) becomes a bit smaller, the positions of the center of the area do not change, as shown in Figs. 3(b) and 3(d). These properties of η demonstrate that the stability and the high efficiency of the JDE can be maintained in our junctions when the length of the junctions is increased. In Fig. 3, the orientation angle α_R of the right AMSC is only taken as $0 \leqslant \alpha_R \leqslant \pi$ since the antisymmetric relation for η in Eq. (9) still holds for the wider and longer junctions with $N_y = 15$ or $N_x = 10$.

Here, we give some discussions on several scales and their relations in our junctions. The first scale is the coherence length $\xi_0 = \hbar v_F/\Delta_0 = 2\sqrt{t_0\mu}/\Delta_0$ in superconductors, which can be calculated as about $283a$ using $t_0 = 1$, $\mu = 2$, and $\Delta_0 = 0.01$. The second scale is the length of NM, which is given by $\Delta x = N_x a$ as shown in Fig. 6. From the two scales, one can find that the short junctions are considered in this paper since we have $\Delta x \ll \xi_0$ even for $N_x = 10$ in Fig. 3. Due to the presence of AMs with RSOC in our junctions, the spin of electrons is not conserved. In this situation, both singlet and triplet superconducting correlations will arise in NM [71,72]. The third scale defined by us is the decay length ξ of the singlet correlation in AM, which is given by $\xi = \hbar v_F/t_J$. For a moderate value of t_J with $t_J = 0.5$, $\xi = \xi_0/50 \approx 5.66a$. When the length of NM increases from $\Delta x = a$ with $N_x = 1$ to $\Delta x = 10a$ with $N_x = 10$, the singlet correlation will decay fast and finally becomes negligible [71,72]. However, the triplet correlation possesses a larger penetration length and will decay slowly with the increase of Δx [71,72]. It will dominate the Josephson effects in our junctions with $\Delta x = 10a$ and in longer junctions with $\Delta x > 10a$.

Now, we discuss the experimental realization of the JDE in our AMSC/NM/AMSC junctions. First, the high efficiency of the JDE can be obtained when t_J is of the order of $10^{-1}t_0$, e.g., $t_J \approx 0.4t_0$ in Fig. 3 or $t_J \approx 0.5t_0$ in Fig. 2(c), which is just the typical magnitude of altermagnetism in AM [54,64]. For RSOC, its value in the AM without coupling to SC is about $t_J/10$ (see the supplemental material of Ref. [54]). The SC on AM will enhance the strength of RSOC due to the breaking of the reflection symmetry in AM/SC heterostructure. The strength of RSOC can also be enhanced by an applied electric field or the substrate beneath AM. Actually, even for $\lambda = t_J/10$, a diode efficiency exceeding 10% can be acquired in our junctions, as discussed above and as shown in Figs. 2 and 3. Second, the detection of the Josephson effect in junctions composed of materials with a different crystallographic orientation is a mature technology in experiment [73]. It is expected that the high efficiency in our junctions can be detected for a given orientation angle of the right AMSC. Finally, we noticed that two theoretical schemes for the field-free superconducting diode have been proposed by the authors of Refs. [33] and [38]. It is worth emphasizing that the field-free diode in these works means that the realization of the diode effect does not need an applied magnetic field. But the periodic arrangement of magnetic dots or the ferromagnetic insulator is still needed in these schemes, which implies that the magnetic

cross-talk in these schemes cannot be avoided. This is distinct from our field-free scheme based upon AMs in which any magnetic field is not needed and the magnetic cross-talk can be completely eliminated.

IV. CONCLUSIONS

We theoretically study the nonreciprocity of supercurrent in the Josephson junctions based upon AMs. The JDE with the high efficiency can be realized without an external field and the ferromagnetic exchange field, which remains stable in a large range of parameter values. The sign change of the diode efficiency can be brought about by rotating the orientation angle in AMSC or altering the magnitudes of altermagnetism and RSOC. The highly efficient JDE can survive well regardless of the width or the length of the junctions. We also analyze the symmetry of the CPRs based on the transformations of the time-reversal, the spin-rotation, and the mirror reflection operations, and we show that the occurrence of the JDE is a result of the combination of both time-reversal symmetry breaking and in-plane inversion breaking. The investigations in this paper will enable the study and application of the field-free JDE based upon AMs.

ACKNOWLEDGMENTS

This work was financially supported by the National Natural Science Foundation of China under Grants No. 12374034, No. 11921005, and No. 11447175, the Innovation Program for Quantum Science and Technology (2021ZD0302403), the Strategic Priority Research Program of Chinese Academy of Sciences (XDB28000000), and the project ZR2023MA005 supported by Shandong Provincial Natural Science Foundation. We acknowledge the High Performance Computing Platform of Peking University for providing computational resources.

APPENDIX A: THE ELECTRONIC STRUCTURE FOR THE NORMAL STATE OF AMSCs

The continuum Hamiltonian for the normal state of the left or right AMSC, i.e., the AM system with RSOC, can be written as

$$h_{\mathrm{AM}} = \sum_{\mathbf{k}} \tilde{\psi}^{+}_{L(R)}(\mathbf{k}) \hat{h}_{\mathrm{AM}}(\mathbf{k}) \tilde{\psi}_{L(R)}(\mathbf{k}), \tag{A1}$$

with $\hat{h}_{\mathrm{AM}}(\mathbf{k}) = \hat{h}_0(\mathbf{k}) + \hat{h}_J(\mathbf{k}) + \hat{h}_\lambda(\mathbf{k})$ and $\tilde{\psi}_{L(R)}(\mathbf{k}) = (c_{L(R)\mathbf{k}\uparrow}, c_{L(R)\mathbf{k}\downarrow})^T$ in the spin space. Here, $\hat{h}_0(\mathbf{k}) = [t_0(k_x^2 + k_y^2) - \mu]\sigma_0$, $\hat{h}_J(\mathbf{k}) = t_J[(k_x^2 - k_y^2)\cos 2\alpha + 2k_x k_y \sin 2\alpha]\sigma_z$, and $\hat{h}_\lambda(\mathbf{k}) = \lambda[(k_y \cos\alpha - k_x \sin\alpha)\sigma_x - (k_x \cos\alpha + k_y \sin\alpha)\sigma_y]$ in the spin space of particles. The orientation angle is denoted by α, where the subscript $l(r)$ is omitted for brevity. The eigenvalue equation for the particles in the normal state can be written as

$$\hat{h}_{AM}(\mathbf{k})\chi(\mathbf{k}) = E\chi(\mathbf{k}). \tag{A2}$$

The energies of the particles can be solved from the eigenvalue equation as

$$E_\pm = t_0(k^2 - \mu) \pm \xi(\mathbf{k}), \tag{A3}$$

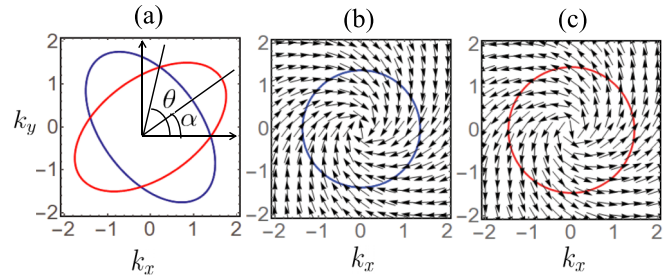

FIG. 4. (a) The elliptical Fermi surfaces of AM without RSOC. Panels (b) and (c) are the circular Fermi surfaces for the E_+ and E_- bands of the two-dimensional electron gas with only RSOC. The black arrows denote the spin of particles in momentum space. The parameters are taken as $t_0 = 1$, $t_J = 0.5$, $\lambda = 0.1$, $\alpha = 0.2\pi$, and $\mu = 2$.

with $\xi(\mathbf{k}) = \frac{1}{\sqrt{2}}\{k^2(t_J^2 k^2 + 2\lambda^2) + t_J^2[(k_x^4 + k_y^4 - 6k_x^2 k_y^2)\cos 4\alpha + 4k_x k_y(k_x^2 - k_y^2)\sin 4\alpha]\}^{1/2}$ and $k^2 = k_x^2 + k_y^2$. The eigenvectors can be written correspondingly as

$$\chi_{+(-)}(\mathbf{k}) = \begin{pmatrix} +(-)ie^{i\alpha}\frac{[\xi(\mathbf{k}) + \hat{h}_{J11(22)}(\mathbf{k})]}{\lambda(k_x + ik_y)} \\ 1 \end{pmatrix}, \tag{A4}$$

with $\hat{h}_{J11(22)}(\mathbf{k})$ being the 11(22) component of the matrix $\hat{h}_J(\mathbf{k})$. The averages of the spin of the particles in the normal state can be calculated using the eigenvectors in Eq. (A4), the components of which are given by

$$\begin{aligned}
\langle s_{x+(-)}\rangle &= +(-)\frac{[\xi(\mathbf{k}) + \hat{h}_{J11(22)}(\mathbf{k})]\lambda(k_y \cos\alpha - k_x \sin\alpha)}{[\xi(\mathbf{k}) + \hat{h}_{J11(22)}(\mathbf{k})]^2 + \lambda^2 k^2}, \\
\langle s_{y+(-)}\rangle &= -(+)\frac{[\xi(\mathbf{k}) + \hat{h}_{J11(22)}(\mathbf{k})]\lambda(k_y \sin\alpha + k_x \cos\alpha)}{[\xi(\mathbf{k}) + \hat{h}_{J11(22)}(\mathbf{k})]^2 + \lambda^2 k^2}, \\
\langle s_{z+(-)}\rangle &= \frac{1}{2}\frac{[\xi(\mathbf{k}) + \hat{h}_{J11(22)}(\mathbf{k})]^2 - \lambda^2 k^2}{[\xi(\mathbf{k}) + \hat{h}_{J11(22)}(\mathbf{k})]^2 + \lambda^2 k^2}.
\end{aligned} \tag{A5}$$

Here, $s_{x+(-)}$, $s_{y+(-)}$, and $s_{z+(-)}$ are the x, y, and z components of spin for the particles with energies $E_{+(-)}$.

To understand the electric structure of the normal state, i.e., the AM with RSOC, we first discuss the electric structures for the system with $\lambda \neq 0$ or $t_J \neq 0$ only. For $\lambda = 0$ and $t_J \neq 0$, the Hamiltonian in Eq. (A1) describes the AM without RSOC. In this case, the Fermi surfaces are two ellipses populated by electrons with the opposite spin due to the altermagnetism in AM [53], as shown in Fig. 4(a). The electrons on the blue ellipse have the spin along the $+z$ direction while those on the red ellipse have the spin along the $-z$ direction. The two Fermi surfaces intersect at $\theta = \alpha + (2n+1)\pi/4$ in the momentum space, with n being an integer number. In particular, for the $d_{x^2-y^2}$-wave altermagnetism with $\alpha = 0$, the two Fermi surfaces intersect at $\theta = (2n+1)\pi/4$, while for the d_{xy}-wave altermagnetism with $\alpha = \pi/4$, the Fermi surfaces intersect at $\theta = n\pi/2$. At the intersection points, the electrons are spin-unpolarized. Otherwise, the electrons are spin-polarized on the Fermi surfaces.

On the other hand, for $t_J = 0$ and $\lambda \neq 0$, the Hamiltonian in Eq. (A1) describes the usual two-dimensional electron gas with only RSOC after the α angle rotation of the

crystallographic axis. In this case, the Fermi surfaces are two concentric circles with different radius as shown in Figs. 4(b) and 4(c). The blue circle is the Fermi surface determined by $E_+ = 0$ while the red circle is the Fermi surface determined by $E_- = 0$. The spin of particles on the two Fermi surfaces is pinned in the xy plane with $\langle s_{z+(-)}\rangle = 0$ due to the presence of RSOC. The spin textures are formed on the two Fermi surfaces due to the spin-momentum locking. The black arrows in Figs. 4(b) and 4(c) denote the spin vectors $(\langle s_{x+}\rangle, \langle s_{y+}\rangle)$ and $(\langle s_{x-}\rangle, \langle s_{y-}\rangle)$ in the whole momentum space. From the plot of the spin vectors in Figs. 4(b) and 4(c), one can obtain the information of the spin distribution on the two Fermi surfaces. The dot product between the momentum and the corresponding spin vector on the Fermi surfaces can be given by $(\langle s_{x+(-)}\rangle, \langle s_{y+(-)}\rangle) \cdot (k_x, k_y) = -(+)\frac{k}{2}\sin\alpha$, which means that the angle between the momentum and the spin is $\alpha + \pi/2$ on the Fermi surface determined by $E_+ = 0$ and is $\alpha - \pi/2$ on the Fermi surface determined by $E_- = 0$. If one takes $\alpha = 0$, the momentum and the spin will be perpendicular, which corresponds to the familiar two-dimensional electron gas system without the α angle rotation of the crystallographic axis [45].

Now, we discuss the electric structure of AM with RSOC, which is the normal state of AMSCs considered in our Josephson junctions. In this situation, $t_J \neq 0$ and $\lambda \neq 0$. The Fermi surfaces consist of two closed curves as shown in Fig. 5. The blue curve in Figs. 5(a) or 5(b) is determined by $E_+ = 0$, while the red curve in Figs. 5(c) or 5(d) is determined by $E_- = 0$. The averages of the spin for particles can be calculated from Eq. (A5). The black arrows in Figs. 5(a)–5(d) denote the spin vectors $\langle(s_{x+}\rangle, \langle s_{y+}\rangle)$, $\langle(s_{x+}\rangle, \langle s_{z+}\rangle)$, $\langle(s_{x-}\rangle, \langle s_{y-}\rangle)$, and $\langle(s_{x-}\rangle, \langle s_{z-}\rangle)$ in the whole momentum space. From the figures, the average spin for particles on the two Fermi surfaces can be observed. Due to the coexistence of altermagnetism and RSOC, the spin of particles will obtain both the in-plane component and the out-of-plane component. In other words, the three components $\langle s_{x+(-)}\rangle$, $\langle s_{y+(-)}\rangle$, and $\langle s_{z+(-)}\rangle$ are all nonzero. However, the in-plane component of spin is dominant only in the zones around $\theta = \alpha + (2n+1)\pi/4$ as shown in Figs. 5(a) and 5(c) while the out-of-plane component is dominant in the other zones. This can also be clearly seen in Figs. 5(b) and 5(d). This is because the spin is unpolarized along the direction $\theta = \alpha + (2n+1)\pi/4$ in the AM without RSOC as discussed above and as shown in Fig. 4(a). In the zones around this direction, the introduction of RSOC will pin the spin in the xy plane. In the other zones, the spin is polarized along the z direction in the AM before introducing RSOC. Hence, the spin will almost retain the polarization after the introduction of a small RSOC.

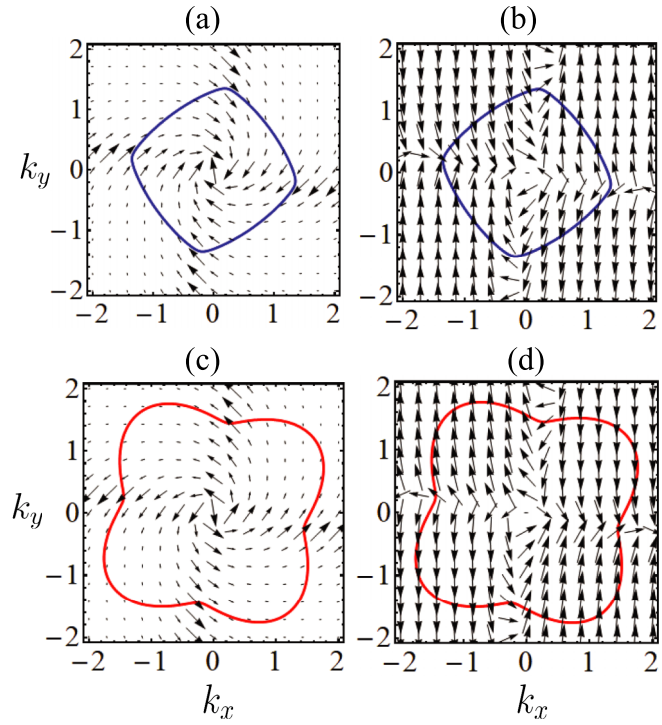

FIG. 5. The Fermi surfaces and the spin structures of electrons in AM with RSOC in momentum space. The Fermi surface denoted by the blue closed line in (a) and (b) is determined by $E_+ = 0$. The Fermi surface denoted by the red closed line in (c) and (d) is determined by $E_- = 0$. The black arrows in (a) and (c) represent the spin vectors $(\langle s_{x+}\rangle, \langle s_{y+}\rangle)$ and $(\langle s_{x-}\rangle, \langle s_{y-}\rangle)$, respectively. The black arrows in (b) and (d) denote the spin vectors $(\langle s_{x+}\rangle, \langle s_{z+}\rangle)$ and $(\langle s_{x-}\rangle, \langle s_{z-}\rangle)$, respectively. The parameters have been taken as $t_0 = 1, t_J = 0.5, \lambda = 0.1, \alpha = 0.2\pi$, and $\mu = 2$.

APPENDIX B: THE DERIVATION OF THE GREEN FUNCTIONS

The continuum Hamiltonian in Eq. (1) can be discretized on the two-dimensional square lattice with the lattice constant a as shown in Fig. 6. From the continuum Hamiltonian in Eq. (1), the matrices in the discrete Hamiltonian in Eq. (3) can be obtained. For clarity, we express the matrices $\check{H}, \check{H}_x, \check{H}_y, \check{H}_{xy}, \check{H}_{x\bar{y}}$ for the left (right) AMSC, and NM in Eq. (3) as $\check{H}_{L(R)}, \check{H}_{L(R)x}, \check{H}_{L(R)y}, \check{H}_{L(R)xy}, \check{H}_{L(R)x\bar{y}}$ and $\check{H}_N, \check{H}_{Nx}, \check{H}_{Ny}, \check{H}_{Nxy}, \check{H}_{Nx\bar{y}}$, respectively. These matrices are given by

$$\check{H}_{L(R)} = \left(\frac{4t_0 - \mu}{a^2}\right)\tau_z \otimes \sigma_0 - \Delta_0[\cos\phi_{l(r)}\tau_y \otimes \sigma_y + \sin\phi_{l(r)}\tau_x \otimes \sigma_y], \tag{B1}$$

$$\check{H}_{L(R)x} = -\frac{t_0}{a^2}\tau_z \otimes \sigma_0 - \frac{t_J\cos 2\alpha_{l(r)}}{a^2}\tau_z \otimes \sigma_z + \frac{i\lambda}{2a}[\cos\alpha_{l(r)}\tau_z \otimes \sigma_y + \sin\alpha_{l(r)}\tau_0 \otimes \sigma_x], \tag{B2}$$

$$\check{H}_{L(R)y} = -\frac{t_0}{a^2}\tau_z \otimes \sigma_0 + \frac{t_J\cos 2\alpha_{l(r)}}{a^2}\tau_z \otimes \sigma_z - \frac{i\lambda}{2a}[\cos\alpha_{l(r)}\tau_0 \otimes \sigma_x - \sin\alpha_{l(r)}\tau_z \otimes \sigma_y], \tag{B3}$$

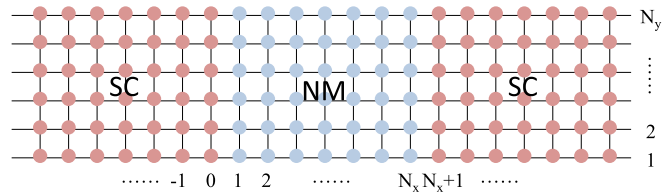

FIG. 6. The two-dimensional square lattice on which the continuum Hamiltonian is discretized.

and

$$\check{H}_{L(R)xy} = -\check{H}_{L(R)x\bar{y}} = -\frac{t_J \sin\alpha_{l(r)}}{2a^2}\tau_z \otimes \sigma_z \tag{B4}$$

for the left (right) AMSC. For the central NM, one has

$$\check{H}_N = \left(\frac{4t_0}{a^2} - \mu\right)\tau_z \otimes \sigma_0, \tag{B5}$$

$$\check{H}_{Nx} = \check{H}_{Ny} = -\frac{t_0}{a^2}\tau_z \otimes \sigma_0. \tag{B6}$$

$$\check{H}_{Nxy} = \check{H}_{Nx\bar{y}} = 0. \tag{B7}$$

The hopping matrices in Eq. (4) can be given by

$$\check{T}_L = \check{T}_R = \mathrm{diag}(t, t, -t, -t). \tag{B8}$$

To facilitate the numerical calculations, we introduce the unitary operator [74]

$$U = e^{\sum_{\mathbf{i}\sigma}[-(\frac{i\phi_l}{2}\psi^+_{L\mathbf{i}\sigma}\psi_{L\mathbf{i}\sigma} + \frac{i\phi_r}{2}\psi^+_{R\mathbf{i}\sigma}\psi_{R\mathbf{i}\sigma})]}, \tag{B9}$$

which can lead to the transformations $U\psi_{L(R)\mathbf{i}\sigma}U^{-1} = e^{i\phi_{l(r)}/2}\psi_{L(R)\mathbf{i}\sigma}$ and $U\psi^+_{L(R)\mathbf{i}\sigma}U^{-1} = e^{-i\phi_{l(r)}/2}\psi^+_{L(R)\mathbf{i}\sigma}$. Then, the transformation on the discrete Hamiltonian H in Eq. (3) will change $\check{H}_{L(R)}$ in Eq. (B1) into

$$\check{H}_{L(R)} = \left(\frac{4t_0 - \mu}{a^2}\right)\tau_z \otimes \sigma_0 - \Delta_0\tau_y \otimes \sigma_y, \tag{B10}$$

and will change the hopping matrices in Eq. (B8) into

$$\check{T}_{L(R)} = \mathrm{diag}(te^{-i\phi_{l(r)}/2}, te^{-i\phi_{l(r)}/2}, -te^{i\phi_{l(r)}/2}, -te^{i\phi_l(r)/2}), \tag{B11}$$

which is the one given by Eq. (4). The other matrices in Eq. (3) are not changed. In other words, the expression of $\check{H}_{L(R)}$ in Eq. (3) is the one in Eq. (B10), while the expressions of $\check{H}_x$, $\check{H}_y$, $\check{H}_{xy}$, and $\check{H}_{x\bar{y}}$ for AMSCs and NM in Eq. (3) are given by Eqs. (B2)–(B6).

In Fig. 6, the junctions have been discretized into a series of columns. Each column contains N_y lattice points. The Hamiltonian for an isolated column in the left (right) AMSC can be given by

$$H_{L(R)11} = \begin{pmatrix} \check{H}_{L(R)} & \check{H}^+_{L(R)y} & & & & \\ \check{H}_{L(R)y} & \check{H}_{L(R)} & \check{H}^+_{L(R)y} & & & \\ & \check{H}_{L(R)y} & \check{H}_{L(R)} & \check{H}^+_{L(R)y} & & \\ & & & \ddots & & \\ & & & & \check{H}^+_{L(R)y} & \\ & & & & \check{H}_{L(R)y} & \check{H}_{L(R)} \end{pmatrix}. \tag{B12}$$

The Hamiltonian for the hopping from one column to its right neighbor column is given by

$$H_{L(R)12} = \begin{pmatrix} \check{H}_{L(R)x} & \check{H}_{L(R)x\bar{y}} & & & & \\ \check{H}_{L(R)xy} & \check{H}_{L(R)x} & \check{H}_{L(R)x\bar{y}} & & & \\ & \check{H}_{L(R)xy} & \check{H}_{L(R)x} & \check{H}_{L(R)x\bar{y}} & & \\ & & & \ddots & & \\ & & & & \check{H}_{L(R)x\bar{y}} & \\ & & & & \check{H}_{L(R)xy} & \check{H}_{L(R)x} \end{pmatrix}. \tag{B13}$$

The Hamiltonian for the hopping from one column to its left neighbor column is given by $H_{L(R)21} = H^+_{L(R)12}$.

For NM, the corresponding matrices are given by

$$H_{N11} = \begin{pmatrix} \check{H}_N & \check{H}^+_{Ny} & & & & \\ \check{H}_{Ny} & \check{H}_N & \check{H}^+_{Ny} & & & \\ & \check{H}_{Ny} & \check{H}_N & \check{H}^+_{Ny} & & \\ & & & \ddots & & \\ & & & & \check{H}^+_{Ny} & \\ & & & & \check{H}_{Ny} & \check{H}_N \end{pmatrix} \tag{B14}$$

and

$$H_{N12} = H_{N21} = 1_{N_y\times N_y} \otimes H_{Nx}. \tag{B15}$$

Below, we derive the surface Green functions of the left and right AMSCs by constructing the Möbius transformation matrix [67]. For the left AMSC, the matrix can be written as

$$X_L = \begin{pmatrix} 0 & H^{-1}_{L12} \\ -H^+_{L12} & [(E + i\gamma) - H_{L11}]H^{-1}_{L12} \end{pmatrix} \tag{B16}$$

with γ being a small positive quantity. The matrix X_L can be diagonalized by the matrix U_L, i.e., $U_L^{-1}X_LU_L = \mathrm{diag}(\lambda_{L1}, \lambda_{L2}, \lambda_{L3}, \dots)$. The eigenvalues satisfy the relation $|\lambda_{L1}| < |\lambda_{L2}| < |\lambda_{L3}| < \cdots$. If we express the matrix U_L as

$$U_L = \begin{pmatrix} U_{L11} & U_{L12} \\ U_{L21} & U_{L22} \end{pmatrix}, \tag{B17}$$

then the surface Green function for the left AMSC is given by $g^r_L = U_{L12}U^{-1}_{L22}$. For the right AMSC, the Möbius transformation matrix can be constructed as

$$X_R = \begin{pmatrix} 0 & (H^+_{R12})^{-1} \\ -H_{R12} & [(E + i\gamma - H_{R11})](H^+_{R12})^{-1} \end{pmatrix}. \tag{B18}$$

Similarly, it can be diagonalized by the matrix U_R. The surface Green function for the right AMSC can be written as $g^r_R = U_{R12}U^{-1}_{R22}$ with the 12 component U_{R12} and 22 component U_{R22} of the matrix U_R.

Next, we use the recursive algorithm to calculate the retarded Green function for the leftmost column of NM. The Green function for the rightmost column of NM is given by

$$\mathcal{G}^r(E, N_x) = \left[E - H_{N11} - \tilde{T}^+_R g^r_R(E)\tilde{T}_R\right]^{-1}, \tag{B19}$$

with $\tilde{T}_R = 1_{N_y\times N_y} \otimes \check{T}_R$. The Green function for the nth column can be obtained by

$$\mathcal{G}^r(E,n) = [E - H_{N11} - H_{N12}\mathcal{G}^r(E,n+1)H_{N21}]^{-1}. \quad \text{(B20)}$$

Then, the retarded Green function for the leftmost column of NM is given by

$$G_N^r(E) = \left[E - H_{N11} - \tilde{T}_L^+ g_L^r(E)\tilde{T} - H_{N12}\mathcal{G}^r(E,2)H_{N21}\right]^{-1}. \quad \text{(B21)}$$

The advanced Green function for the leftmost column of NM is obtained by $G_N^a(E) = [G_N^r(E)]^+$.

After obtaining the surface Green functions $g_L^r(E)$ and $g_R^r(E)$, the retarded Green function $G_N^r(E)$, and the advanced Green function $G_N^a(E)$, the Green function in Eq. (6) can be expressed as

$$G_{NL}^r(E) = G_N^r(E)\tilde{T}_L^+ g_L^r(E), \quad \text{(B22)}$$

$$G_{NL}^a(E) = G_N^a(E)\tilde{T}_L^+ g_L^a(E), \quad \text{(B23)}$$

with $g_L^a(E) = [g_L^r(E)]^+$. Using the fluctuation-dissipation theorem, the lesser Green function $G_{NL}^<(E)$ is given by

$$G_{NL}^<(E) = -f(E)\left[G_{NL}^r(E) - G_{NL}^a(E)\right]. \quad \text{(B24)}$$

Substituting the expression of $G_{NL}^<(E)$ into Eq. (6), the Josephson current can be numerically calculated.

APPENDIX C: THE SYMMETRY ANALYSIS

For $t_J = 0$ and $\lambda \neq 0$, the left and right AMSCs are time-reversal invariant due to the absence of altermagnetism. We introduce the time-reversal operation $\mathcal{T}$, which can transform the annihilation operator $c_{\mathbf{k}\sigma}$ in the following manner:

$$\mathcal{T} c_{\mathbf{k}\sigma}\mathcal{T}^{-1} = \sigma c_{-\mathbf{k}\bar{\sigma}}, \quad \text{(C1)}$$

with $\sigma = \uparrow\downarrow$ or $\pm$. Under the time-reversal transformation, the Hamiltonian for the left (right) AMSC will become

$$\mathcal{T} H_{L(R)}(\alpha_{L(R)}, \phi_{L(R)})\mathcal{T}^{-1} = H_{L(R)}(\alpha_{L(R)}, -\phi_{L(R)}). \quad \text{(C2)}$$

Since the time-reversal operation will invert the Josephson current in the junctions, we have

$$I(\alpha_L, \alpha_R, \phi) = -I(\alpha_L, \alpha_R, -\phi). \quad \text{(C3)}$$

This relation means that the critical current for the positive direction and that for the negative direction will possess the same value. There will be no JDE for the junctions with only RSOC and without altermagnetism.

For $t_J \neq 0$ and $\lambda = 0$, the time-reversal symmetry is broken due to the presence of altermagnetism. In this situation, we introduce the spin-rotation operation about the y axis by a π angle, i.e., $\mathcal{R}_y(\pi)$, which can transform the annihilation operator $c_{\mathbf{k}\sigma}$ in the following manner:

$$\mathcal{R}_y(\pi) c_{\mathbf{k}\sigma}\mathcal{R}_y^{-1}(\pi) = \bar{\sigma} c_{\mathbf{k}\bar{\sigma}}. \quad \text{(C4)}$$

The Hamiltonian for the left (right) AMSC is invariant under the joint operation $\mathcal{X} = \mathcal{R}_y(\pi)\mathcal{T}$, which leads to

$$\mathcal{X} H_{L(R)}(\alpha_{L(R)}, \phi_{L(R)})\mathcal{X}^{-1} = H_{L(R)}(\alpha_{L(R)}, -\phi_{L(R)}). \quad \text{(C5)}$$

Accordingly, the Josephson current will satisfy the following relation:

$$I(\alpha_L, \alpha_R, \phi) = -I(\alpha_L, \alpha_R, -\phi). \quad \text{(C6)}$$

This relation implies that the JDE will not exist in the junctions with only altermagnetism and without RSOC, which is irrespective of the orientation angles α_L and α_R.

From the above discussions, one can find that the coexistence of RSOC and altermagnetism is the necessary condition for the JDE in our AMSC/NM/AMSC junctions. Actually, another condition is also necessary for the JDE, which is the different orientation between the left AMSC and the right AMSC. To show this, we introduce the mirror reflection operations about the xz plane and the yz plane, which can transform the annihilation operator $c_{\mathbf{k}\sigma}$ in the following manner:

$$\mathcal{M}_{xz} c_{(k_x,k_y)\sigma}\mathcal{M}_{xz}^{-1} = \sigma c_{(k_x,-k_y)\bar{\sigma}}, \quad \text{(C7)}$$

$$\mathcal{M}_{yz} c_{(k_x,k_y)\sigma}\mathcal{M}_{yz}^{-1} = -ic_{(-k_x,k_y)\bar{\sigma}}. \quad \text{(C8)}$$

Under these operations, the transformations of the Hamiltonian for the left (right) AMSC are given by

$$\mathcal{M}_{xz} H_{L(R)}(t_J, \lambda, \alpha_{L(R)}, \phi_{L(R)})\mathcal{M}_{xz}^{-1} = H_{L(R)}(-t_J, \lambda, -\alpha_{L(R)}, \phi_{L(R)}) \quad \text{(C9)}$$

and

$$\mathcal{M}_{yz} H_{L(R)}(t_J, \lambda, \alpha_{L(R)}, \phi_{L(R)})\mathcal{M}_{yz}^{-1} = H_{R(L)}(-t_J, \lambda, -\alpha_{L(R)}, \phi_{L(R)}). \quad \text{(C10)}$$

As a result, the joint operation $\mathcal{Y} = \mathcal{M}_{xz}\mathcal{M}_{yz}$ will transform the Hamiltonian in the following way:

$$\mathcal{Y} H_{L(R)}(\alpha_{L(R)}, \phi_{L(R)})\mathcal{Y}^{-1} = H_{R(L)}(\alpha_{L(R)}, \phi_{L(R)}). \quad \text{(C11)}$$

The operation $\mathcal{M}_{xz}$ will not change the Josephson current, but the operation $\mathcal{M}_{yz}$ will invert the current through exchanging the superconducting phases for the left AMSC and the right AMSC. At the same time, the orientation angles in the left AMSC and the right AMSC are also exchanged. Then, we have the relation

$$I(\alpha_L, \alpha_R, \phi) = -I(\alpha_R, \alpha_L, -\phi). \quad \text{(C12)}$$

If one takes $\alpha_L = \alpha_R = \alpha$, the relation $I(\alpha, \phi) = -I(\alpha, -\phi)$ will hold. This means that the JDE will be absent in the AMSC/NM/AMSC junctions with the same orientation angle for the left AMSC and the right AMSC, although both RSOC and altermagnetism are present. The joint operation $\mathcal{Y}$ actually represents the in-plane inversion. The relation in Eq. (C11) shows that the Josephson junctions respect the in-plane inversion symmetry when AMSCs have the same orientation angle. In other words, the in-plane inversion symmetry must be broken in order to obtain the JDE in the AMSC/NM/AMSC junctions based upon AMs.

Finally, we discuss the special case of $\alpha_L = 0$. The numerical results for this situation have been presented in the main text. We introduce the joint operation $\mathcal{Z} = \mathcal{T}\mathcal{M}_{xz}$. For the left (right) AMSC, the Hamiltonian can be transformed in

the following way:

$$\mathcal{Z}H_{L(R)}(\alpha_{L(R)}, \phi_{L(R)})\mathcal{Z}^{-1} = H_{L(R)}(2\pi - \alpha_{L(R)}, -\phi_{L(R)}). \tag{C13}$$

Then, we have the relation $I(\alpha_L, \alpha_R, \phi) = -I(2\pi - \alpha_L, 2\pi - \alpha_R, -\phi)$ for the Josephson current. For $\alpha_L = 0$, the relation will degenerate into $I(\alpha_R, \phi) = -I(2\pi - \alpha_R, -\phi)$. This suggests that the values of the critical current for the positive direction and the negative direction will be exchanged if the orientation angle in the right AMSC is changed from α_R to $2\pi - \alpha_R$. The diode efficiency η will change its sign correspondingly, i.e., $\eta(\alpha_R) = -\eta(2\pi - \alpha_R)$, which is consistent with the numerical results in Fig. 2(b). In addition, if $\alpha_R = \pi$, we can obtain $I(\pi, \phi) = -I(\pi, -\phi)$, which leads to $\eta(\pi) = 0$ as shown in Fig. 2(b).

In the above discussions, we do not give the transformations of the Hamiltonian H_N for NM under time reversal, spin rotation, and mirror reflection operations since H_N will be invariant under these operations. The invariance of H_N will not influence the above symmetry analysis about the CPRs.

[1] F. Ando, Y. Miyasaka, T. Li, J. Ishizuka, T. Arakawa, Y. Shiota, T. Moriyama, Y. Yanase, and T. Ono, Observation of superconducting diode effect, Nature (London) **584**, 373 (2020).

[2] J.-X. Lin, P. Siriviboon, H. D. Scammell, S. Liu, D. Rhodes, K. Watanabe, T. Taniguchi, J. Hone, M. S. Scheurer, and J. I. A. Li, Zero-field superconducting diode effect in small-twist-angle trilayer graphene, Nat. Phys. **18**, 1221 (2022).

[3] H. Narita, J. Ishizuka, R. Kawarazaki, D. Kan, Y. Shiota, T. Moriyama, Y. Shimakawa, A. V. Ognev, A. S. Samardak, Y. Yanase, and T. Ono, Field-free superconducting diode effect in noncentrosymmetric superconductor/ferromagnet multilayers, Nat. Nanotechnol. **17**, 823 (2022).

[4] S. Ilić and F. S. Bergeret, Theory of the supercurrent diode effect in rashba superconductors with arbitrary disorder, Phys. Rev. Lett. **128**, 177001 (2022).

[5] Y. Hou, F. Nichele, H. Chi, A. Lodesani, Y. Wu, M. F. Ritter, D. Z. Haxell, M. Davydova, S. Ilić, O. Glezakou-Elbert, A. Varambally, F. S. Bergeret, A. Kamra, L. Fu, P. A. Lee, and J. S. Moodera, Ubiquitous superconducting diode effect in superconductor thin films, Phys. Rev. Lett. **131**, 027001 (2023).

[6] N. F. Q. Yuan and L. Fu, Supercurrent diode effect and finite-momentum superconductors, Proc. Natl. Acad. Sci. USA **119**, e2119548119 (2022).

[7] J. J. He, Y. Tanaka, and N. Nagaosa, A phenomenological theory of superconductor diodes James, New J. Phys. **24**, 053014 (2022).

[8] A. Daido and Y. Yanase, Superconducting diode effect and nonreciprocal transition lines, Phys. Rev. B **106**, 205206 (2022).

[9] H. F. Legg, D. Loss, and J. Klinovaja, Superconducting diode effect due to magnetochiral anisotropy in topological insulators and Rashba nanowires, Phys. Rev. B **106**, 104501 (2022).

[10] B. Zinkl, K. Hamamoto, and M. Sigrist, Symmetry conditions for the superconducting diode effect in chiral superconductors, Phys. Rev. Res. **4**, 033167 (2022).

[11] T. de Picoli, Z. Blood, Y. Lyanda-Geller, and J. I. Väyrynen, Superconducting diode effect in quasi-one-dimensional systems, Phys. Rev. B **107**, 224518 (2023).

[12] P. Hosur and D. Palacios, Proximity-induced equilibrium supercurrent and perfect superconducting diode effect due to band asymmetry, Phys. Rev. B **108**, 094513 (2023).

[13] A. Daido, Y. Ikeda, and Y. Yanase, Intrinsic superconducting diode effect, Phys. Rev. Lett. **128**, 037001 (2022).

[14] R. Kealhofer, H. Jeong, A. Rashidi, L. Balents, and S. Stemmer, Anomalous superconducting diode effect in a polar superconductor, Phys. Rev. B **107**, L100504 (2023).

[15] M. Chazono, S. Kanasugi, T. Kitamura, and Y. Yanase, Piezoelectric effect and diode effect in anapole and monopole superconductors, Phys. Rev. B **107**, 214512 (2023).

[16] J. Yun, S. Son, J. Shin, G. Park, K. Zhang, Y. J. Shin, J.-G. Park, and D. Kim, Magnetic proximity-induced superconducting diode effect and infinite magnetoresistance in a van der Waals heterostructure, Phys. Rev. Res. **5**, L022064 (2023).

[17] T. Karabassov, I. V. Bobkova, A. A. Golubov, and A. S. Vasenko, Hybrid helical state and superconducting diode effect in superconductor/ferromagnet/topological insulator heterostructures, Phys. Rev. B **106**, 224509 (2022).

[18] J. J. He, Y. Tanaka, and N. Nagaosa, The supercurrent diode effect and nonreciprocal paraconductivity due to the chiral structure of nanotubes, Nat. Commun. **14**, 3330 (2023).

[19] S. Chahid, S. Teknowijoyo, I. Mowgood, and A. Gulian, High-frequency diode effect in superconducting Nb_3Sn microbridges, Phys. Rev. B **107**, 054506 (2023).

[20] H. Wu, Y. Wang, Y. Xu, P. K. Sivakumar, C. Pasco, U. Filippozzi, S. S. P. Parkin, Y.-J. Zeng, T. McQueen, and M. N. Ali, The field-free Josephson diode in a van der Waals heterostructure, Nature (London) **604**, 653 (2022).

[21] C. Baumgartner, L. Fuchs, A. Costa, S. Reinhardt, S. Gronin, G. C. Gardner, T. Lindemann, M. J. Manfra, P. E. Faria, Jr., D. Kochan, J. Fabian, N. Paradiso, and C. Strunk, Supercurrent rectification and magnetochiral effects in symmetric Josephson junctions, Nat. Nanotechnol. **17**, 39 (2022).

[22] A. Banerjee, M. Geier, M. A. Rahman, C. Thomas, T. Wang, M. J. Manfra, K. Flensberg, and C. M. Marcus, Phase asymmetry of andreev spectra from cooper-pair momentum, Phys. Rev. Lett. **131**, 196301 (2023).

[23] C. Ciaccia, R. Haller, A. C. C. Drachmann, T. Lindemann, M. J. Manfra, C. Schrade, and C. Schonenberger, Gate-tunable Josephson diode in proximitized InAs supercurrent interferometers, Phys. Rev. Res. **5**, 033131 (2023).

[24] B. Pal, A. Chakraborty, P. K. Sivakumar, M. Davydova, A. K. Gopi, A. K. Pandeya, J. A. Krieger, Y. Zhang, M. Date, S. Ju, N. Yuan, N. B. M. Schröter, L. Fu, and S. S. P. Parkin, Josephson diode effect from Cooper pair momentum in a topological semimetal, Nat. Phys. **18**, 1228 (2022).

[25] J. Díez-Mérida, A. Díez-Carlón, S. Y. Yang, Y.-M. Xie, X.-J. Gao, J. Senior, K. Watanabe, T. Taniguchi, X. Lu, A. P. Higginbotham, K. T. Law, and D. K. Efetov, Symmetry-broken

Josephson junctions and superconducting diodes in magic-angle twisted bilayer graphene, Nat. Commun. **14**, 2396 (2023).
[26] M. Trahms, L. Melischek, J. F. Steiner, B. Mahendru, I. Tamir, N. Bogdnoff, O. Peters, G. Reecht, C. B. Winkelmann, F. von Oppen, and K. J. Franke, Diode effect in Josephson junctions with a single magnetic atom, Nature (London) **615**, 628 (2023).
[27] S. Matsuo, T. Imoto, T. Yokoyama, Y. Sato, T. Lindemann, S. Gronin, G. C. Gardner, M. J. Manfra, and S. Tarucha, Josephson diode effect derived from short-range coherent coupling, Nat. Phys. **19**, 1636 (2023).
[28] J. Hu, C. Wu, and X. Dai, Proposed design of a Josephson diode, Phys. Rev. Lett. **99**, 067004 (2007).
[29] A. A. Kopasov, A. G. Kutlin, and A. S. Mel'nikov, Geometry controlled superconducting diode and anomalous Josephson effect triggered by the topological phase transition in curved proximitized nanowires, Phys. Rev. B **103**, 144520 (2021).
[30] K. Misaki and N. Nagaosa, Theory of the nonreciprocal Josephson effect, Phys. Rev. B **103**, 245302 (2021).
[31] K. Halterman, M. Alidoust, R. Smith, and S. Starr, Supercurrent diode effect, spin torques, and robust zero-energy peak in planar half-metallic trilayers, Phys. Rev. B **105**, 104508 (2022).
[32] M. Davydova, S. Prembabu, and L. Fu, Universal Josephson diode effect, Sci. Adv. **8**, eabo0309 (2022).
[33] J. Jiang, M. V. Milošević, Y.-L. Wang, Z.-L. Xiao, F. M. Peeters, and Q.-H. Chen, Field-free superconducting diode in a magnetically nanostructured superconductor, Phys. Rev. Appl. **18**, 034064 (2022).
[34] Ya. V. Fominov and D. S. Mikhailov, Asymmetric higher-harmonic SQUID as a Josephson diode, Phys. Rev. B **106**, 134514 (2022).
[35] Y. Zhang, Y. Gu, P. Li, J. Hu, and K. Jiang, General theory of Josephson diodes, Phys. Rev. X **12**, 041013 (2022).
[36] R. S. Souto, M. Leijnse, and C. Schrade, Josephson diode effect in supercurrent interferometers, Phys. Rev. Lett. **129**, 267702 (2022).
[37] Y. Tanaka, B. Lu, and N. Nagaosa, Theory of giant diode effect in d-wave superconductor junctions on the surface of a topological insulator, Phys. Rev. B **106**, 214524 (2022).
[38] T. H. Kokkeler, A. A. Golubov, and F. S. Bergeret, Field-free anomalous junction and superconducting diode effect in spin-split superconductor/topological insulator junctions, Phys. Rev. B **106**, 214504 (2022).
[39] Q. Cheng and Q.-F. Sun, Josephson diode based on conventional superconductors and a chiral quantum dot, Phys. Rev. B **107**, 184511 (2023).
[40] Y.-F. Sun, Y. Mao, and Q.-F. Sun, Design of Josephson diode based on magnetic impurity, Phys. Rev. B **108**, 214519 (2023).
[41] J. F. Steiner, L. Melischek, M. Trahms, K. J. Franke, and F. von Oppen, Diode effects in current-biased Josephson junctions, Phys. Rev. Lett. **130**, 177002 (2023).
[42] A. Maiani, K. Flensberg, M. Leijnse, C. Schrade, S. Vaitiekenas, and R. S. Souto, Nonsinusoidal current-phase relations in semiconductor-superconductor-ferromagnetic insulator devices, Phys. Rev. B **107**, 245415 (2023).
[43] J.-X. Hu, Z.-T. Sun, Y.-M. Xie, and K. T. Law, Josephson diode effect induced by valley polarization in twisted bilayer graphene, Phys. Rev. Lett. **130**, 266003 (2023).
[44] B. Lu, S. Ikegaya, P. Burset, Y. Tanaka, and N. Nagaosa, Tunable Josephson diode effect on the surface of topological insulators, Phys. Rev. Lett. **131**, 096001 (2023).
[45] A. Costa, J. Fabian, and D. Kochan, Microscopic study of the Josephson supercurrent diode effect in Josephson junctions based on two-dimensional electron gas, Phys. Rev. B **108**, 054522 (2023).
[46] J.-D. Pillet, S. Annabi, A. Peugeot, H. Riechert, E. Arrighi, J. Griesmar, and L. Bretheau, Josephson diode effect in Andreev molecules, Phys. Rev. Res. **5**, 033199 (2023).
[47] R. Hess, H. F. Legg, D. Loss, and J. Klinovaja, Josephson transistor from the superconducting diode effect in domain wall and skyrmion magnetic racetracks, Phys. Rev. B **108**, 174516 (2023).
[48] E. W. Hodt and J. Linder, On-off switch and sign change for a nonlocal Josephson diode in spin-valve Andreev molecules, Phys. Rev. B **108**, 174502 (2023).
[49] M. Gupta, G. V. Graziano, M. Pendharkar, J. T. Dong, C. P. Dempsey, C. Palmstrøm, and V. S. Pribiag, Gate-tunable superconducting diode effect in a three-terminal Josephson device, Nat. Commun. **14**, 3078 (2023).
[50] T. Jungwirth, X. Marti, P. Wadley, and J. Wunderlich, Antiferromagnetic spintronics, Nat. Nanotechnol. **11**, 231 (2016).
[51] J.-M. Hu, Z. Li, L.-Q. Chen, and C.-W. Nan, High-density magnetoresistive random access memory operating at ultralow voltage at room temperature, Nat. Commun. **2**, 553 (2011).
[52] I. I. Mazin, Editorial: Altermagnetism–A new punch line of fundamental magnetism, Phys. Rev. X **12**, 040002 (2022).
[53] L. Šmejkal, J. Sinova, and T. Jungwirth, Beyond conventional ferromagnetism and antiferromagnetism: A phase with nonrelativistic spin and crystal rotation symmetry, Phys. Rev. X **12**, 031042 (2022).
[54] L. Šmejkal, A. B. Hellenes, R. González-Hernández, J. Sinova, and T. Jungwirth, Giant and tunneling magnetoresistance in unconventional collinear antiferromagnets with nonrelativistic spin-momentum coupling, Phys. Rev. X **12**, 011028 (2022).
[55] L. Šmejkal, J. Sinova, and T. Jungwirth, Emerging research landscape of altermagnetism, Phys. Rev. X **12**, 040501 (2022).
[56] J. Krempaský, L. Šmejkal, S. W. D'Souza, M. Hajlaoui, G. Springholz, K. Uhlířová, F. Alarab, P. C. Constantinou, V. Strocov, D. Usanov *et al.*, Altermagnetic lifting of Kramers spin degeneracy, Nature (London) **626**, 517 (2024).
[57] S. Lee, S. Lee, S. Jung, J. Jung, D. Kim, Y. Lee, B. Seok, J. Kim, B. G. Park, L. Šmejkal, C.-J. Kang, and C. Kim, Broken kramers degeneracy in altermagnetic MnTe, Phys. Rev. Lett. **132**, 036702 (2024).
[58] X. Zhou, W. Feng, R.-W. Zhang, L. Šmejkal, J. Sinova, Y. Mokrousov, and Y. Yao, Crystal thermal transport in altermagnetic RuO_2, Phys. Rev. Lett. **132**, 056701 (2024).
[59] H. Bai, Y. C. Zhang, Y. J. Zhou, P. Chen, C. H. Wan, L. Han, W. X. Zhu, S. X. Liang, Y. C. Su, X. F. Han, F. Pan, and C. Song, Efficient spin-to-charge conversion via altermagnetic spin splitting effect in antiferromagnet RuO_2, Phys. Rev. Lett. **130**, 216701 (2023).
[60] Q. Cheng and Q.-F. Sun, Orientation-dependent Josephson effect in spin-singlet superconductor/altermagnet/ spin-triplet superconductor junctions, Phys. Rev. B **109**, 024517 (2024).
[61] C. Sun, A. Brataas, and J. Linder, Andreev reflection in altermagnets, Phys. Rev. B **108**, 054511 (2023).

[62] M. Papaj, Andreev reflection at the altermagnet-superconductor interface, Phys. Rev. B **108**, L060508 (2023).

[63] J. A. Ouassaou, A. Brataas, and J. Linder, dc Josephson effect in altermagnets, Phys. Rev. Lett. **131**, 076003 (2023).

[64] C. W. J. Beenakker and T. Vakhtel, Phase-shifted Andreev levels in an altermagnet Josephson junction, Phys. Rev. B **108**, 075425 (2023).

[65] Y.-X. Li and C.-C. Liu, Majorana corner modes and tunable patterns in an altermagnet heterostructure, Phys. Rev. B **108**, 205410 (2023).

[66] D. Zhu, Z.-Y. Zhuang, Z. Wu, and Z. Yan, Topological superconductivity in two-dimensional altermagnetic metals, Phys. Rev. B **108**, 184505 (2023).

[67] Q. Cheng, Q. Yan, and Q.-F. Sun, Spin-triplet superconductor-quantum anomalous Hall insulator-spin-triplet superconductor Josephson junctions: 0-π transition, φ_0 phase, and switching effects, Phys. Rev. B **104**, 134514 (2021).

[68] Q.-F. Sun and X. C. Xie, Quantum transport through a graphene nanoribbon-superconductor junction, J. Phys.: Condens. Matter **21**, 344204 (2009).

[69] J. Song, H. Liu, J. Liu, Y.-X. Li, R. Joynt, Q.-F. Sun, and X. C. Xie, Quantum interference in topological insulator Josephson junctions, Phys. Rev. B **93**, 195302 (2016).

[70] Q. Cheng, Y. Zhang, K. Zhang, B. Jin, and C. Zhang, Symmetry analysis of transport properties in helical superconductor junctions, J. Phys.: Condens. Matter **29**, 085601 (2017).

[71] F. S. Bergeret, A. F. Volkov, and K. B. Efetov, Long-range proximity effects in superconductor-ferromagnet structures, Phys. Rev. Lett. **86**, 4096 (2001).

[72] A. Kadigrobov, R. I. Shekhter, and M. Jonson, Quantum spin fluctuations as a source of long-range proximity effects in diffusive ferromagnet-superconductor structures, Europhys. Lett. **54**, 394 (2001).

[73] B. Chesca, D. Doenitz, T. Dahm, R.P. Huebener, D. Koelle, R. Kleiner, Ariando, H. J. H. Smilde, and H. Hilgenkamp, Observation of Andreev bound states in $YBa_2Cu_3O_{7-x}$/Au/Nb ramp-type Josephson junctions, Phys. Rev. B **73**, 014529 (2006).

[74] Q.-F. Sun, B.-G. Wang, J. Wang, and T.-H. Lin, Electron transport through a mesoscopic hybrid multiterminal resonant-tunneling system, Phys. Rev. B **61**, 4754 (2000).